RESEARCH COMMUNICATION

Cytochrome *c* oxidase-modulatory near-infrared light penetration into the human brain: Implications for the noninvasive treatment of ischemia/reperfusion injury

Paul T. Morse[1] | Dennis J. Goebel[2] | Junmei Wan[1] | Samuel Tuck[1,3] | Lara Hakim[1] | Charlotte L. Hüttemann[1] | Moh H. Malek[4] | Icksoo Lee[5] | Thomas H. Sanderson[3] | Maik Hüttemann[1,6]

[1]Center for Molecular Medicine and Genetics, Wayne State University, Detroit, Michigan

[2]Department of Ophthalmology, Visual and Anatomical Sciences, Wayne State University, Detroit, Michigan

[3]Department of Emergency Medicine, University of Michigan Medical School, Ann Arbor, Michigan

[4]Department of Health Care Sciences, Eugene Applebaum College of Pharmacy & Health Sciences, Wayne State University, Detroit, Michigan

[5]College of Medicine, Dankook University, Cheonan-si, Republic of Korea

[6]Department of Biochemistry, Microbiology and Immunology, Wayne State University, Detroit, Michigan

Correspondence

Maik Hüttemann, Center for Molecular Medicine and Genetics, Wayne State University School of Medicine, Detroit, MI 48201.
Email: mhuttema@med.wayne.edu

Funding information

Office of the Assistant Secretary of Defense for Health Affairs through the Peer Reviewed Medical Research Program, Grant/Award Number: W81XWH-16-1-0175; U.S. National Institutes of Health, Grant/Award Number: R42NS105238

Abstract

Near-infrared light (IRL) has been evaluated as a therapeutic for a variety of pathological conditions, including ischemia/reperfusion injury of the brain, which can be caused by an ischemic stroke or cardiac arrest. Strategies have focused on modulating the activity of mitochondrial electron transport chain (ETC) enzyme cytochrome *c* oxidase (COX), which has copper centers that broadly absorb IRL between 700 and 1,000 nm. We have recently identified specific COX-inhibitory IRL wavelengths that are profoundly neuroprotective in rodent models of brain ischemia/reperfusion through the following mechanism: COX inhibition by IRL limits mitochondrial membrane potential hyperpolarization during reperfusion, which otherwise causes reactive oxygen species (ROS) production and cell death. Prior to clinical application of IRL on humans, IRL penetration must be tested, which may be wavelength dependent. In the present study, four fresh (unfixed) cadavers and isolated cadaver tissues were used to examine the transmission of infrared light through human biological tissues. We conclude that the transmission of 750 and 940 nm IRL through 4 cm of cadaver head supports the viability of IRL to treat human brain ischemia/reperfusion injury and is similar for skin with different skin pigmentation. We discuss experimental difficulties of working with fresh cadavers and strategies to overcome them as a guide for future studies.

Abbreviations: AIF, apoptosis-inducing factor; Bcl-2, B-cell lymphoma 2; COX, cytochrome *c* oxidase; CSF, cerebrospinal fluid; ETC, electron transport chain; IRL, infrared light; PAR, poly ADP-ribose; PARP, poly ADP-ribose polymerase; ROS, reactive oxygen species; $\Delta\Psi_m$, mitochondrial membrane potential.

1 | INTRODUCTION

Globally, 15 million people have a stroke each year, with 80% of those being focal ischemic strokes.[1,2] In addition, over 356,000 people experience a cardiac arrest annually in the United States alone, causing global brain ischemia.[3] Cellular signaling mechanisms tightly link energy production to energy demand.[4] Any perturbation of this balance, such as caused by ischemia, results in numerous adaptive and deleterious changes, which drive a feedforward loop that pushes neuronal cells toward cell death. Ischemia results in energy depletion, halting vital biological processes.[5] The only way to salvage the affected brain tissue is rapid restoration of blood flow to the ischemic region by enzymatic removal or mechanical thrombectomy of the blood clot for focal stroke or by resuscitation after cardiac arrest. However, in addition to the ischemic insult, which causes cell death, restoration of blood flow results in additional reperfusion injury. A primary cause underlying reperfusion injury and cell death is mitochondrial reactive oxygen species (ROS) that are generated through the following sequence of events.[6] Ischemia leads to energy depletion and calcium release, which causes changes in the posttranslational modification state of the electron transport chain (ETC) enzymes. As an example, we recently showed that cytochrome c is phosphorylated on serine 47 under normal, nonischemic conditions but becomes dephosphorylated during ischemia,[7] likely mediated by calcium-activated phosphatases. Serine phosphorylation leads to controlled respiration, whereas dephosphorylation drives maximal ETC flux during reperfusion when oxygen and nutrients are reintroduced into the tissue. This in turn leads to mitochondrial membrane potential ($\Delta\Psi_m$) hyperpolarization and bursts of ROS,[8] further amplified by reverse electron flow.[9] Furthermore, dephosphorylation of cytochrome c increases caspase activation, further sensitizing cells to apoptosis.[7,10] Other components of the ETC may also change their posttranslational modification status during the course of ischemia and reperfusion, as was shown for cytochrome c oxidase (COX) in cardiomyocytes.[11,12]

Clinical trials targeting ROS with scavengers have failed,[13,14] likely due to the inherent difficulties in delivering adequate concentrations of ROS scavengers to the appropriate subcellular sites within the crucial early minutes of reflow, when $\Delta\Psi_m$ hyperpolarization peaks in the brain.[15] In addition, drugs act systemically, limiting the use of high concentrations due to possible side effects elsewhere in the body. Therefore, a nonpharmacological approach that does not rely on blood flow and acts immediately and locally where needed would be preferable because it would allow targeting of the early reperfusion period. One such approach is to apply near-infrared light (IRL) to the affected area with the added benefit in that it is a noninvasive and local treatment.

The IRL spectrum ranges from 700 to 1,000 nm and has been evaluated as a possible noninvasive therapeutic for a wide variety of central nervous system conditions, including stroke.[16] IRL overlaps with an "optical window" in biological tissue that occurs due to the comparatively low absorbances of hemoglobin above 650 nm and water below 1,000 nm.[17] This allows IRL to noninvasively penetrate into tissues, including the brain. Biologically, the most relevant chromophore of IRL is COX due to its two enzymatically active copper centers,[18] which broadly absorb IRL between 700 and 1,000 nm as can be seen in the COX absorption spectrum.[19] Previous research often used stimulatory IRL wavelengths to improve neurological function after stroke by stimulating COX activity to increase ATP production.[20,21] While a commonly studied wavelength of IRL, 810 nm, does stimulate COX and mitochondrial function, it is important to note that this is not universally true of the entire spectrum. We have recently discovered that irradiation with IRL in the range of 750 and 950 nm inhibits COX activity,[22] thus providing a unique tool for the treatment of reperfusion injury following ischemia by reducing ETC flux, $\Delta\Psi_m$, and ROS. These effects were seen using purified COX protein, intact mitochondria, intact cells, and in rats. Importantly, we observed that treatment with these COX-inhibitory, but not with the COX-activating, wavelengths were highly neuroprotective in rat models of global brain ischemia and focal stroke with a single application administered for 2 or 4 hr acutely after the ischemic insult.[22,23] After 8 min of global brain ischemia following reperfusion, rats lost 88% of hippocampal CA1 neurons, whereas application of 2 hr of IRL only resulted in 11–35% neuronal loss for 750 nm, 950 nm, and the combination.[22] Interestingly, applying the IRL treatment to the more severe (90 min) focal ischemia model and extending the treatment duration from 2 to 4 hr during reperfusion more than doubled the protective effect and resulted in an infarct size reduction from 21 to 52%, respectively.[23] Although more research is needed, it is

possible that inhibition of late-stage ROS production and inflammatory cell conversion through ROS signaling may account for this finding.

In order to consider human applications of IRL, major questions remain regarding the feasibility of this approach to treat ischemia/reperfusion injury in the human brain. Small animal models, commonly mice and rats, have been used to show the promise of IRL to treat neurological dysfunction, but it remains unknown whether the IRL would penetrate deeply enough into the human brain to have a therapeutic effect. As a first step to address this question for therapeutic COX-inhibitory IRL, the current study used unfixed cadavers to analyze the transmission of IRL through the head into the brain. The use of fresh cadavers poses unique methodological challenges that we discuss in the section "Lessons learned from working with cadavers and limitations of the current study" in addition to the underlying cellular processes in brain ischemia/reperfusion injury that IRL seeks to treat.

2 | MATERIALS AND METHODS

2.1 | Laser system and measurement apparatus

A custom-built laser assembly containing a 750 nm-emitting IRL diode unit and 940 nm-emitting IRL diode unit was obtained from Lumitex, Inc., Strongsville, Ohio. Each laser diode unit has a fiber optic cable with an Sub Miniature version A (SMA) connector on the light-emitting end and its own digital user control menu to adjust the IRL power produced at the emitting end. The IRL output power of the custom 750-nm laser unit was controlled by adjusting the amperage in the unit's user controls menu. An amperage to 750-nm IRL power calibration curve was generated by increasing the amperage in 0.1 A increments from 1.5 A to 5.0 A and measuring the resultant power of 750-nm light in watts using a Newport Optical Power/Energy Meter (Model 842-PE; Newport Corporation, Irvine, California). The light output of the 940-nm laser unit is directly controlled by adjusting the power in its user controls menu and was verified using the Newport Meter. Both 750- and 940-nm IRL diode units emit light as a narrow cone with a Gaussian emission pattern. To take measurements, an optical power meter (PM160; ThorLabs, Newton, New Jersey) was mounted on an adjustable tray. The optical power meter was covered with a barrier made from transparent non-IRL-absorbing plastic bags (Ziploc Brand Snack Bags; SC Johnson, Racine, Wisconsin) cut and heat sealed to precisely fit the optical power meter to prevent tissue and liquid from directly contacting the detector surface. The fiber optic cables from the laser diodes were attached with clamps above the adjustable tray in such a way as to maintain the beam onto the detector of the optical power meter in a direct light path as shown in Figure 1. The adjustable tray with attached optical power meter and fiber optic cables were mounted onto a 360° articulating arm (AmazonBasics Premium 32 Inch Monitor Stand, Aluminum; Amazon, Seattle, Washington), attached to a freely movable cart containing the laser units, to allow for the setup to maintain its position once correctly inserted into the cadaver.

2.2 | Cadaver donation

Whole, unfixed cadavers were made available for research by the Body Bequest program at Wayne State University School of Medicine, Department of Ophthalmology, Visual and Anatomical Sciences. Donor consent for educational and research purposes was obtained prior to death through the Body Bequest program in accordance with the Uniform Anatomical Gift Act of Michigan (Act. No. 368, Public Acts of 1978, Article 10). After transport to Wayne State University, cadavers were stored at 4°C in the mortuary refrigerator in the on-site morgue until surgical dissection and transmission measurements were performed. The surgical dissection and transmission measurements were carried out at 16°C in the dissection suite in the on-site morgue.

2.3 | Site selection and surgical dissection

Each of the four lobes of the brain (frontal, parietal, occipital, and temporal) were evaluated as IRL delivery points. The frontal position was standardized by measuring 4 cm superior to the eyebrows, avoiding the air space of the frontal sinus.[24–26] The parietal position was standardized by locating the most superior portion of the head. The occipital position was standardized by measuring directly inferior to the external occipital protuberance. The temporal position was standardized by locating the pterion. Cadaver heads were carefully shaved prior to dissection. To access all the positions selected for measurement, a craniotomy was performed. Anatomical arch-shaped windows into the brains were generated above the temple by first removing the skin and soft tissue of the head using a scalpel. Next, the underlying bone was removed using a Stryker 810 Autopsy Saw (Stryker Corporation, Kalamazoo, Michigan), exposing the dura
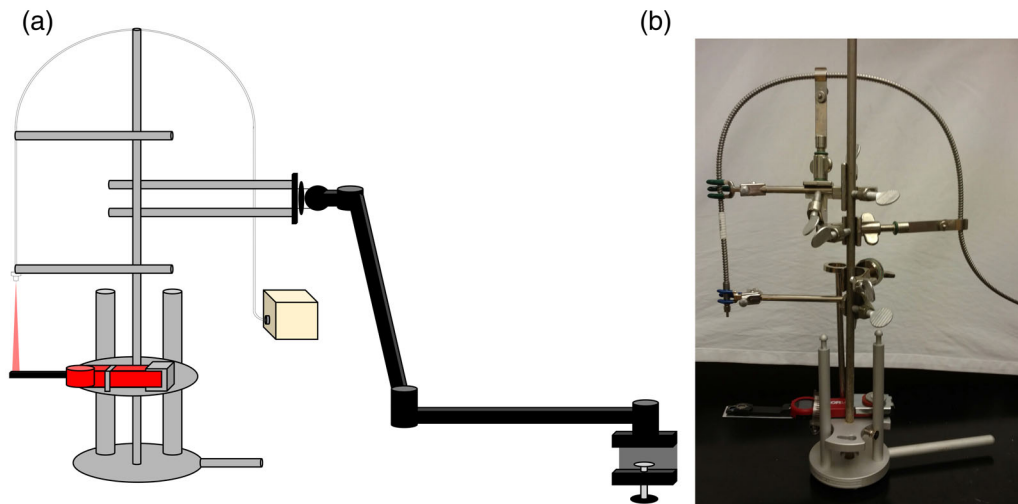
FIGURE 1 Measurement apparatus setup. (a) Cartoon illustration (not to scale) of the setup used for cadaver measurements. Represented are the height-adjustable tray, mounted optical power meter, fiber optic cable, 360° articulating arm with mount, and light source. (b) Picture of the actual measurement apparatus setup with mounted optical meter (without the 360° articulating arm and IRL source)
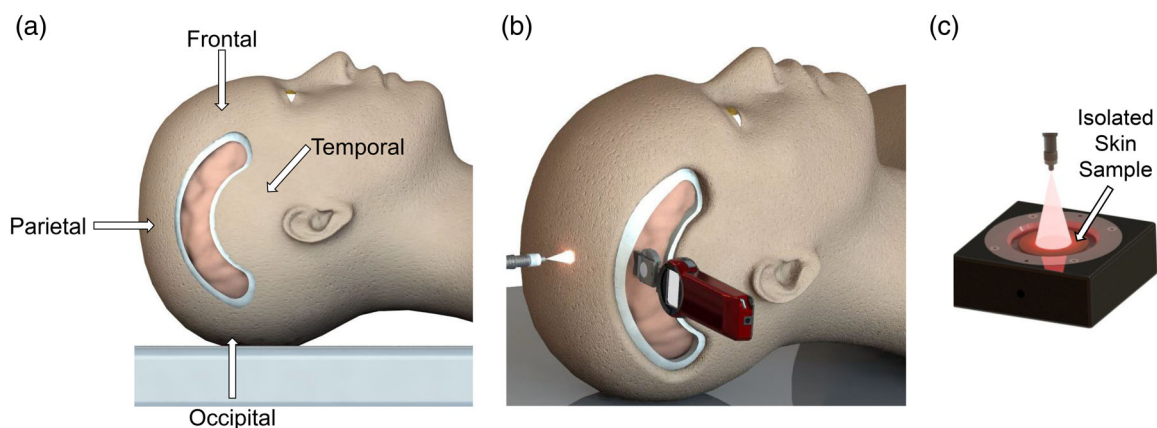

FIGURE 2 Schematic representation of fresh cadaver dissection, whole head light transmission measurements, and isolated tissue light transmission measurements. (a) Visual representation of standard arch dissection performed on cadavers. Measurement positions (frontal, parietal, occipital, and temporal) are labeled. Lasers emitting 750 or 940-nm IRL were shone onto the spots indicated with the arrows. Optical power detectors were embedded into the brain in direct line with the emitted light at a depth of 4 cm. (b) Visual representation of infrared light transmission measurements into the parietal lobe of a cadaver. Measurement apparatus (not shown) ensured that the light from the fiber optic output point was beamed in a direct light path onto the detector surface of the optical power meter, which was embedded in the cadaver's head. The detector surface was covered (not shown) with a transparent, non-IRL-absorbing shield made from plastic bags. The fiber optic was positioned 2 cm above the cadaver's skin, and the optical power meter was embedded 4 cm in the head. Other lobes (frontal, occipital, and temporal) were similarly measured. (c) Visual representation of IRL transmission measurements through a skin sample isolated from a cadaver. The detector surface of the optical power meter was covered (not shown) with a transparent, non-IRL-absorbing shield made from plastic wrap. Isolated tissue layers (skin shown here) were placed on the shielded detector surface. Fiber optic was positioned 3 cm above the detector surface of the optical power meter. Other isolated tissue layers (fat, muscle, bone, and brain) were similarly measured

mater. Figure 2a,b illustrates the standard dissection and the measurement positions. Immediately prior to light measurements, a micro-durotomy was performed, and the underlying brain tissue was incised to allow for easy insertion of an optical power meter (PM160).

2.4 | Infrared light transmission measurements into intact cadaver heads

After generating the anatomical window into the brain of each cadaver, the cadaver was positioned such that

gravity pulled the brain toward the skull in order to eliminate air gaps between the brain and the skull in the desired measurement position. Next, the measurement apparatus was lined up in preparation of being inserted into the desired measurement position described above. Immediately prior to insertion of the optical power meter, a micro-durotomy was performed, and the underlying brain tissue was incised to allow for easy insertion laterally into the cadaver's brain, resulting in a distance of 4 cm from the skin of the head into the brain. The assembled measurement apparatus described above ensured that light from the fiber optic cables was directed at the detector surface of the optical power meter in a direct light path even while embedded into the cadaver's brain. In all measurement positions, the fiber optic cables (the light-emitting ends) were oriented at a distance 2 cm away from the cadaver's head, and the optical power meter light sensor arm was embedded at a depth of 4 cm into the cadaver's head. Figure 2b illustrates a representative diagram of measuring light transmitted through the parietal lobe. Once the optical power meter was embedded into a cadaver's head, five background readings with the laser diodes turned off were recorded prior to every experimental transmission reading. In each case, all five background readings were identical (0.0 ± 0.0 µW). To perform an experimental transmission measurement, one of the laser diodes (750 or 940 nm) was turned on and operated continuously for the duration of the measurement at either 2 or 4 watts. Five measurements were taken at each position with each power setting. After measuring light transmission, tissue thickness measurements of the skin, subcutaneous fat, muscle, and bone in the light path were taken using digital calipers (100-333-8B; iGAGING, San Clemente, California). Further dissection was performed, if necessary, to take the tissue thickness measurements.

2.5 | Isolated cadaver tissue collection

Isolated cadaver soft-tissue samples were collected from one African American and one Caucasian cadaver by using a scalpel to score an initial 4 cm by 4 cm square incision of soft tissue anterior to the ear over the temple region. These tissue squares were then collected by cutting down to the skull bones (zygomatic, sphenoid, temporal). This resulted in soft-tissue samples containing skin, subcutaneous fat, and temporalis muscle. From one of the cadavers, isolated bone and brain tissue samples were also collected. After removing the overlying soft-tissue layers to expose the skull bones over the temple (zygomatic, sphenoid, temporal), a 4 cm by 4 cm square of bone was isolated using a Stryker Autopsy Saw. The underlying gray

matter of the temporal lobe of the brain was isolated using a scalpel. Isolated cadaver soft-tissue samples were collected as part of the surgical dissection for intact head light transmission measurements or after finishing intact head light transmission measurements. Isolated soft-tissue samples were wrapped in damp paper towels, placed in sealed plastic bags, and stored on ice until the measurements were performed up to 3 hr later.

2.6 | Infrared light transmission measurements through cadaver tissue layers

Optical power measurements for isolated cadaver tissue layers (African American and Caucasian skin, subcutaneous fat, temporalis muscle, bone, and gray matter of the brain) were performed with a Newport Optical Power/Energy Meter (Model 842-PE). As before, the custom laser diode system capable of emitting light at 750 and 940 nm was used. The fiber optic cables from the laser diodes were positioned 3 cm above the detector surface of the optical power meter in such a way that all light from the laser diodes fell onto the center of the detector. While performing experiments, the optical power meter was covered with a barrier made from non-IRL-absorbing plastic (Total Home Stretch-Tite Plastic Wrap; CVS Pharmacy, Woonsocket, Rhode Island) in order to prevent tissue and liquid from contacting the detector surface. The 4 cm by 4 cm square isolated cadaver tissue samples were cut into circles of a diameter of 1.7 cm and placed onto the detector. Figure 2c illustrates a representative diagram of measuring light transmitted through an isolated skin sample. Next, five background readings with the laser diodes shut off were recorded prior to every experimental transmission reading. In each case, all five background readings were identical (0.000 ± 0.000 W). To perform an experimental transmission measurement, one of the laser diodes (750 or 940 nm) was turned on and operated continuously for the duration of the measurement at either 0.5 or 1 watt. Five measurements were taken at each position with each power setting. After measuring penetration through the soft-tissue layers collectively (skin, subcutaneous fat, and temporalis muscle), the various layers were separated using a scalpel, and penetration through each layer was measured separately. The transmission measurements were performed at 16°C.

2.7 | IRL skin reflection

Reflection and backscattering measurements for human skin were performed with an integrating light sphere

(Model 70461; Oriel Instruments, Stratford, Connecticut) to collect reflected and backscattered light onto a Newport Optical Power/Energy Meter (Model 842-PE). As above, the custom laser diode system emitting light at 750 and 940 nm was used. The fiber optic cables from the laser diodes were fed into the input port of the integrating light sphere and were positioned 3 cm away from the sample port. One of the laser diodes (either 750 or 940 nm) was used continuously for the duration of the measurement at 1 watt. Subsequently, five background readings were recorded with the laser diodes turned on and the sample port of the integrating light sphere uncovered prior to every experimental transmission reading. In each case, all five background readings were identical (0.000 ± 0.000 W). Two skin samples were placed against the sample port of the integrating light sphere. Five measurements were taken with each sample. The reflection and backscattering measurements were performed at 16°C.

2.8 | Statistical analyses

Similar to other light penetration studies[27,31] using human cadavers and ex vivo tissues, data are reported for each subject separately due to significant differences in the physical composition, including the thickness of tissue (e.g., skin, fat, bone, muscle) of the cadavers. Data of the multiple individual IRL measurements are shown as averages ± SD in Figure 3.

3 | RESULTS

3.1 | Infrared light transmission measurements into intact cadaver heads

Transmission measurements of 750- and 940-nm IRL through intact, unfixed cadaver heads were performed on two African American female cadavers, one Caucasian female, and one Caucasian male cadaver. Donor information is presented in Table 1. Surgical dissection and
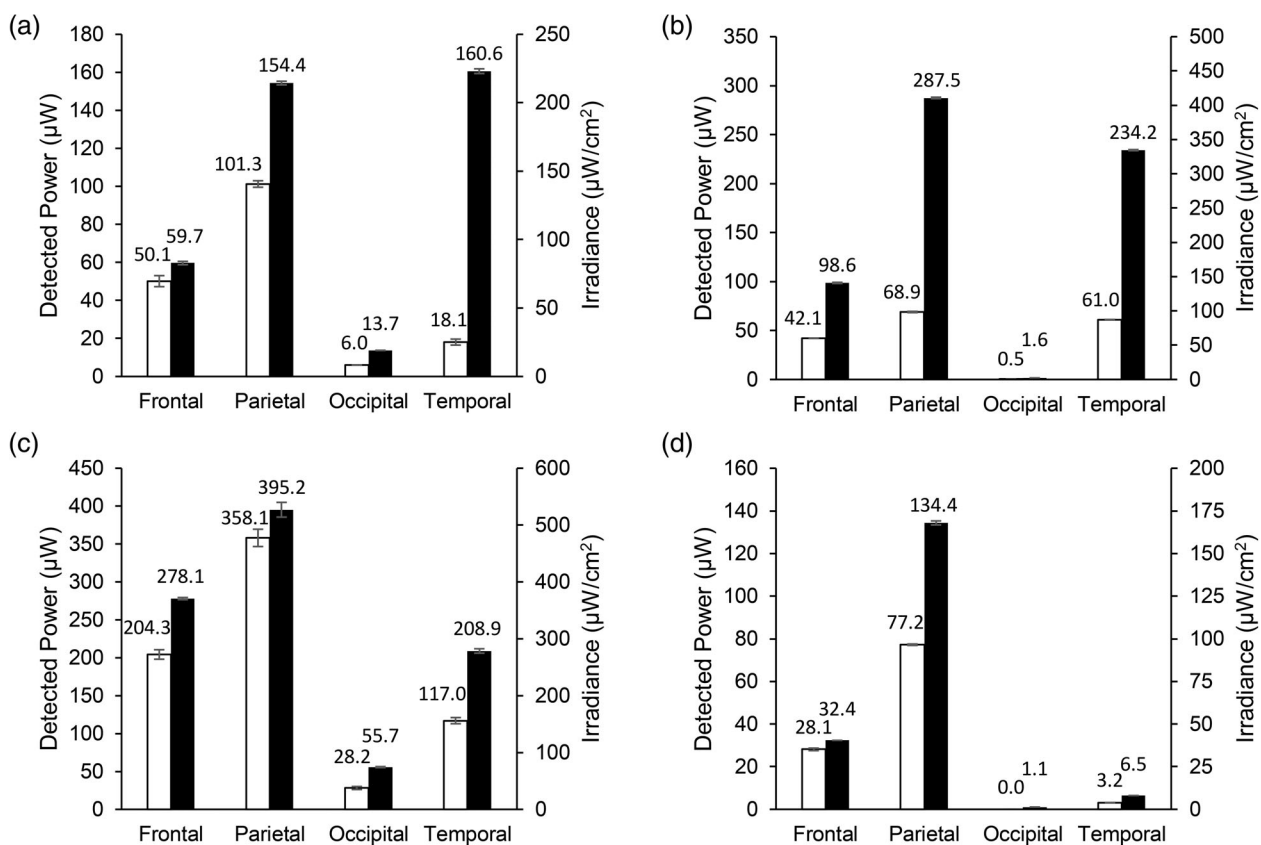

FIGURE 3 Transmission of infrared light through whole, unfixed cadaver heads. Detected power of light in microwatts through 4 cm of whole, unfixed cadaver heads. Conversion of the detected power data to irradiance in microwatts per square centimeter based on the area of the optical power meter used is shown on the secondary y-axis. Data labels represent detected power in microwatts. Empty bars represent a 4-watt input of 750-nm light. Filled bars represent a 4-watt input of 940-nm light. (a) Cadaver 1, (b) Cadaver 2, (c) Cadaver 3, and (d) Cadaver 4 are shown. Error bars represent SD

TABLE 1 Demographic characteristics of donors

Cadaver	Age	Sex	Race	Weight (kg)	Height (cm)	BMI (kg/m^2)	Days since death
1	77	Female	African American	67.1	165.1	24.6	16
2	90	Female	Caucasian	46.2	152.4	19.9	10
3	82	Female	African American	77.1	165.1	28.3	24
4	57	Male	Caucasian	86.2	172.7	28.9	30

Note: Days since Death is calculated as the day of death being day 0, that is, IRL penetration experiments were performed on the day specified in the last column.

transmission measurements were performed between 10 and 30 days after death of the donor. Transmission of IRL through the head into the frontal, parietal, occipital, and temporal lobes was examined. The detected power in microwatts of 750- or 940-nm light with an input power of 4 watts transmitted through 4 cm of unfixed cadaver heads is shown in Figure 3. The experiments were also performed with an input power of 2 watts, which resulted in about 50% of the detected power when compared to the input power of 4 watts (results not shown), indicating a linear relationship between laser output power and IRL detected with the IRL power meter. When comparing the light transmission into a particular lobe of the brain for a given cadaver, the detected power of 940-nm light was higher than that of 750-nm light. Additionally, we noted differences in IRL transmission between the different measurement positions. For 750 nm, the highest power of light was detected through the parietal lobe in all four cadavers. For 940 nm, the highest power of light was detected through the parietal lobe in three out of four cadavers, with the temporal lobe being higher in the remaining cadaver (Figure 3a). The lowest power of light was detected through the occipital lobe in all four cadavers for both wavelengths due to blood accumulation and air gaps (see Section 4). These values are included for completeness but represent a profound underestimation of IRL penetration. Anatomical information regarding the cadavers is shown in Table 2.

3.2 | Infrared light transmission measurements through isolated tissue layers

Transmission measurements of 750- and 940-nm IRL through tissue layers isolated from cadavers was performed on African American and Caucasian skin, subcutaneous fat, temporalis muscle, skull bone, and gray matter brain samples. Samples were collected between 10 and 30 days after death of the donor, and transmission measurements were taken on the same day. The detected power in watts of 750- or 940-nm light with a laser output power of 1 watt transmitted through the isolated tissue

layers is shown in Figure 4. The experiment was also performed with an input power of 0.5 watts (results not shown), which resulted in about 50% reduction of detected power when compared to the input power of 1 watt, confirming a linear relationship between laser output and IRL detected inside the brain at a given distance. When comparing the transmission of 750-nm IRL with 940 nm for the tissue layer samples, the detected power of 940-nm IRL was higher than that of 750 nm, except for the subcutaneous fat layer. The African American skin and Caucasian skin samples had similar levels of transmission with 0.482 watts of 750-nm and 0.511 watts of 940-nm light detected through 0.116 cm of African American skin and 0.470 watts of 750-nm and 0.544 watts of 940-nm light detected through 0.098 cm of Caucasian skin. The subcutaneous fat and temporalis muscle samples had similar thicknesses of 0.505 and 0.509 cm, respectively. Higher powers of IRL were detected through the subcutaneous fat than the temporalis muscle. Anatomical information regarding the tissue layer thicknesses is available in Table 3.

3.3 | IRL skin reflection and backscattering is low

To estimate the loss of IRL due to reflection and backscattering from the skin, skin samples were placed in the sample window of an optical integrating light sphere and then irradiated with 1 watt with 750 and 940 nm (see Section 2). For both wavelengths, IRL reflected and backscattered was less than 3% of input IRL (Figure 5).

4 | DISCUSSION

4.1 | Lessons learned from working with cadavers and limitations of the current study

There were multiple lessons our team learned when working with cadavers. First, pooling blood dramatically

TABLE 2 Anatomical features of unfixed cadaver heads

| Cadaver	Position	Skin thickness (cm)	Fat thickness (cm)	Muscle thickness (cm)	Bone thickness (cm)	Brain thickness (cm)	Total tissue thickness (cm)
1	Frontal	0.098	0.245	0.041	0.696	2.920	4.000
	Parietal	0.117	0.719	0.043	0.846	2.275	4.000
	Occipital	0.111	0.802	0.037	1.319	1.731	4.000
	Temporal	0.102	0.318	0.512	0.350	2.718	4.000
2	Frontal	0.046	0.160	0.032	0.446	3.316	4.000
	Parietal	0.169	0.201	0.013	0.866	2.751	4.000
	Occipital	0.149	0.299	0.026	0.700	2.826	4.000
	Temporal	0.035	0.200	0.347	0.305	3.113	4.000
3	Frontal	0.166	0.269	0.133	0.439	2.993	4.000
	Parietal	0.191	0.672	0.052	0.519	2.566	4.000
	Occipital	0.182	0.587	0.096	0.875	2.260	4.000
	Temporal	0.189	0.509	0.436	0.414	2.452	4.000
4	Frontal	0.178	0.329	0.033	0.909	2.551	4.000
	Parietal	0.248	0.343	0.095	0.385	2.929	4.000
	Occipital	0.323	0.571	0.120	0.593	2.393	4.000
	Temporal	0.238	1.423	0.466	0.376	1.497	4.000
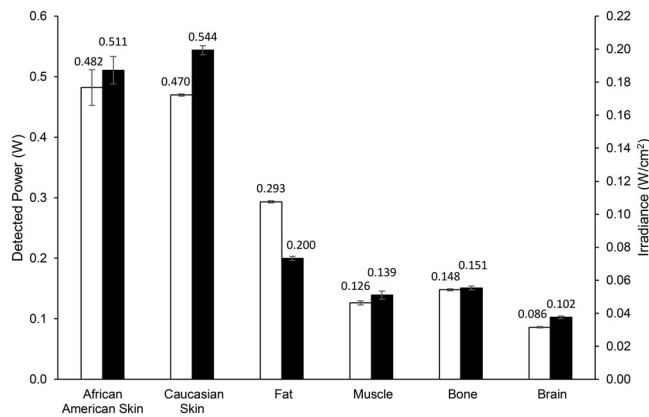
FIGURE 4 Transmission of infrared light through isolated, unfixed cadaver tissue layers. Detected power of light in watts through isolated, unfixed cadaver tissue layers collected from heads. Conversion of the detected power data to irradiance in microwatts per square centimeter based on the area of the optical power meter used is shown on the secondary y-axis. Data labels represent detected power in microwatts. White bars represent a 1-watt input of 750-nm light. Black bars represent a 1-watt input of 940-nm light. Error bars represent SD

TABLE 3 Anatomical features of representative unfixed tissue layers isolated from cadavers

Tissue layer	Thickness (cm)
African American skin	0.116
Caucasian skin	0.098
Fat	0.505
Muscle	0.509
Bone	0.479
Brain	0.215

reduced IRL transmission. Previous publications have demonstrated that blood is a major absorber of IRL,[28] and a higher blood fraction in the measured tissue results in reduced penetration.[29] With the postmortem loss of the pumping action of the cardiovascular system, blood begins to leak out and settle. Between 10 and 30 days passed from the day of death to when IRL transmission measurements were taken. Additionally, in all cases, cadavers were stored face up. The time period between day of death and IRL transmission measurement, along with the position in which the cadavers were stored, caused blood to settle in the posterior areas. This could be visually observed by inspecting the cadaver prior to measurement. The posterior areas of skin were tinted red, as if they were contused, while the anterior areas of skin appeared normal. Cutting into these posterior red skin regions released liquid blood and exposed coagulated blood within the tissue. Notably, for the current study, the posterior side of the skull was similarly affected, which likely reduced IRL transmission through the head
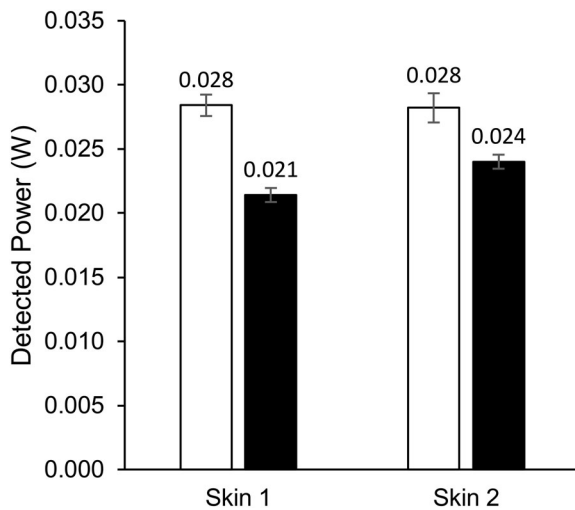
FIGURE 5 Reflection and backscattering measurements of IRL from human skin. Detected power of light in microwatts shows that reflected or backscattered from human skin only results in a minor loss of IRL. White and black bars represent a 1-watt input of 750 nm and 940 nm, respectively. Error bars represent SD

into the occipital lobe, resulting in the low IRL transmission values at this measurement position. The occipital values were included for completeness and to show limitations when working with fresh cadavers. Additionally, the issue of pooling blood increased the susceptibility of the skin to burns. We performed safety tests by increasing the IRL input power up to a maximal laser power of 8 watts by simultaneously operating both the 750- and 940-nm lasers at 4 watts and visually checking the skin for burns. While there were no burns present under these conditions for the frontal, parietal, and temporal measurement positions, we occasionally noticed burns in the occipital position concurrent with the presence of pooled blood. To partially mitigate the issues regarding pooling of blood, it was necessary to prop a cadaver's shoulders up on a wooden beam prior to dissection and continue through IRL transmission measurements to ensure that excess blood drained away from the head instead of into it. It has been proposed that there may even be beneficial, indirect effects of IRL irradiation of blood aside from its effects on COX activity.[30] In living organisms, the blood flow eliminates the issues seen with pooling blood compared to working with cadavers and may even be able to help circulate the benefits of therapeutic IRL, as well as dispersing heat generated at the skin by the IRL input points on the skin, limiting the risk of skin burns.[31]

Second, air gaps in the head caused by the dissection reduced IRL transmission. The micro-durotomy performed during the surgical dissection to embed the optical power meter generated air gaps due to leakage of the cerebrospinal fluid (CSF). In living tissue, the brain is encased in CSF, which provides cushioning. Some of the remaining CSF in the cadavers was lost when the micro-durotomy was performed. This allowed air to enter into the subarachnoid space, introducing two additional tissue–airgap–tissue interfaces, which lowers IRL transmission due to reflection or provided a space for blood to accumulate, exacerbating the issue of blood pooling. Both scenarios lead to a dramatic reduction in IRL penetration and thus an underestimation of transmitted IRL. To mitigate this, cadavers were positioned and rotated in such a way to have gravity pull the brain against the skull prior to transmission measurements in a given position, with the goal of eliminating or at least limiting air gaps created from CSF leakage.

Third, measurements on cadavers and cadaveric tissues should be performed as soon as possible after the dissection and sample collection. While this is the case for all the data shown here, one cadaver was stored overnight at 4°C following dissection of one hemisphere with the hope that additional experiments (not shown) would be able to be performed the following day on the other hemisphere of the head, which was not analyzed on the first day. Despite best attempts to preserve the specimen, gross tissue integrity deteriorated overnight, and the experimental plans were abandoned. We thus recommend to complete IRL penetration studies in a single day in 6 hr or less.

4.2 | Interpreting the data

Light transmission through turbid media depends on both absorption and scattering. Skin and fibrous tissues have high scattering parameters. Tissue types with a higher number of mitochondria or lysosomes will have higher Rayleigh scattering due to the increased density of lipid membranes.[17] To date, much of the literature on tissue penetration was performed on fixed cadaver tissue or decapitated animal tissue.[27,31] Additionally, it is common to simulate the transmission of light through biological tissues based on parameters optimized from prepared tissue samples.[32–34] It is not well understood how the optical properties of postmortem, isolated, or fixed tissues differ from living tissue. The failures of several IRL clinical trials to show clinical benefit in human patients[20,35,36] has prompted several questions about how IRL administration devices are designed and other practical considerations, such as where and how it is applied best and how much light penetrates through the skin into the deeper structures of the human brain.

Originally, we hypothesized that the temple would be the optimal position for IRL delivery to the brain as it is centrally next to the temporal lobe and is the area with

the thinnest part of the skull.[37–39] However, this was not the case as the IRL transmission through the head into the parietal lobe was consistently higher than that into the temporal lobe. This is likely due to the presence of the temporalis muscle, a major muscle of mastication, that varies in thickness.[40] In contrast, on the top of the scalp, there is only a thin aponeurosis layer.[41] This evidence would suggest that, rather than the thickness of the bone, it is the thickness of the muscle and the amount of blood that primarily determines the amount of light that will penetrate into the brain. Unsurprisingly, our occipital results are in contrast with Jagdeo et al., who studied the transmission of 830- and 633-nm light through fixed cadaver head sections, which contain hardly any blood and no pooled blood, and found a higher percent penetration of 830-nm light through the occipital head region than the frontal and temporal head regions.[27] They also used wavelengths that are different from ours, and their results in other experiments similarly indicated that blood is a major attenuator of IRL transmission through biological tissue.

The distance of 4 cm was chosen because ongoing large animal work with young adult pigs undergoing cardiac arrest and resuscitation demonstrates neuroprotection in the hippocampus (unpublished). This indicates that therapeutic doses of IRL can be achieved at this depth into the brain. It is therefore important to know what power densities are present at this depth that produce neuroprotection in vivo. For whole cadaver heads, we consistently found that 940-nm light transmitted better than 750-nm light through 4 cm of tissue. However, the ratio between the transmission of 940-nm IRL and the transmission of 750-nm IRL was variable, indicating the possibility of tissue-specific differences in optical properties, which we evaluated with the isolated tissue layer measurements. Interestingly, Jagdeo et al. also studied the transmission of IRL through living human hands as a model of the head. For the 830-nm IRL, they found that 0.096% penetrated a hand of 2.5 cm thickness, while 0.014% penetrated a hand of 3.0 cm thickness. For comparison purposes, the maximum percent transmission of IRL presented here is 358.1 microwatts of 750-nm light and 395.2 microwatts of 940-nm light detected through 4 cm of unfixed cadaver heads into the parietal lobe with an input of 4 watts, resulting in transmissions of 0.009 and 0.010%, respectively. The fact that IRL transmission values using unfixed cadaver heads fell within the same order of magnitude as living tissue should be encouraging.

The isolated tissue layer measurements, which showed that IRL transmitted better through fat than muscle when the samples were roughly equivalent in thickness, corroborated the observations from the whole cadaver head measurements where transmission of IRL through the head into the parietal lobe was higher than that of the temporal lobe. The isolated cadaver tissue experiments also allowed for comparison between different skin tones. Importantly, there were similar levels of transmission of our two IRL wavelengths between the African American and Caucasian skin samples, indicating that therapeutic IRL would be equally effective for patients with different skin pigmentation.

Another group, Henderson et al., evaluated multiple IRL LED and laser units through isolated human skin samples and 3.0 cm of sheep heads in addition to other samples.[31] For the 3.0 cm of sheep head transmission measurements, the conditions in their study that would be most comparable to the ones here are the use of a single-wavelength 810-nm laser with an actual power input of 4.00 watts and single-wavelength 980-nm laser with an actual power input of 6.22 watts, both operating continuously like ours. For the 3.0-cm sheep head transmission measurements, they detected 2.90 and 1.23% transmitted IRL for the 810-nm laser and 980-nm lasers, respectively. These values are larger than the largest percent transmissions reported in this study, which were 0.009% of 750-nm light and 0.010% of 940-nm light with an input power of 4 watts through 4 cm of unfixed cadaver head into the parietal lobe. These differences can be explained by the additional centimeter of tissue thickness used in this study, differences in biological transmission between different infrared wavelengths, and differences in the specific tissue composition and thicknesses of sheep heads versus human heads.

Other publications have suggested that most IRL is lost in the skin, with about 90% attenuation in the first 2 mm.[42,43] Our results here demonstrate slightly improved transmission, with about 50% being lost in the first 1–1.2 mm. We also estimated the amount of power lost due to reflection and backscattering of the IRL from the skin, concluding that this represents only a minor contribution. It is generally believed that IRL must penetrate at least 4 cm into the head in order to mediate a clinical effect for neurological disorders.[31] Overall, the measurements shown here demonstrate that IRL can be detected at depths of at least 4 cm into unfixed cadaver heads with a single IRL delivery point. Therefore, adding additional IRL delivery points with an overlapping transmission volume would increase the power detectable at 4 cm or at even deeper distances.

4.3 | COX-inhibitory IRL as a treatment for brain ischemia/reperfusion injury of the brain

It has previously been established that ATP production and mitochondrial ROS generation are controlled by the mitochondrial membrane potential ($\Delta\Psi_m$), which is itself maintained by inhibitory phosphorylations of the protein complexes of the ETC under physiological conditions[6,44,45]: Under such normal conditions, these inhibitory phosphorylations are present, which keeps $\Delta\Psi_m$ at optimal intermediate levels of around 100–140 mV. This results in efficient ATP production and low ROS generation, the latter of which increases exponentially at membrane potentials exceeding 140 mV. When the tissue is subjected to ischemia, phosphorylations are lost. Upon reperfusion, for example after a blood clot is removed or after a patient is resuscitated following cardiac arrest, blood flow and oxygen delivery are restored to the formerly ischemic area. The loss of the inhibitory modifications now drives maximal ETC flux, which results in $\Delta\Psi_m$ hyperpolarization, triggering ROS bursts and cell death cascades.[6,46] While endogenous antioxidant mechanisms exist to control ROS levels, drastic increases in ROS, commonly seen during stroke, overwhelm these natural defenses. ROS also trigger numerous cell-signaling pathways as part of the cellular response to stroke, which can further drive neuronal death.

One of the major cell-signaling pathways engaged after stroke is the poly ADP-ribose polymerase (PARP) family in the nucleus. PARP-1 knockout was shown to reduce infarct size in a mouse model of stroke.[47] Further research has uncovered that ROS-mediated damage of DNA induces PARP-1 activation,[48] contributing to mitochondrial–nuclear crosstalk. Glutamate toxicity and subsequent intraneuronal calcium accumulation exacerbate this process and further enhance PARP-1 activity.[49] This results in the conversion of NAD^+ to polymers of poly ADP-ribose (PAR), causing ATP depletion.[50] The formation of PAR is also implicated in further downstream signaling by interacting with DNA damage checkpoint proteins and caspases.[51,52] Additionally, PARP-1 activation changes gene expression and energy utilization that push neurons toward cell death following stroke.[53]

PARP-1 activation also causes the translocation of apoptosis-inducing factor (AIF) from the mitochondria to the nucleus.[54] AIF then goes on to cause chromatin condensation and DNA fragmentation in both caspase-independent and caspase-dependent processes.[55] Similar to PARP-1, AIF knockdown results in reduced infarct sizes in animal models of stroke.[56] Mitochondrial permeabilization, which then releases pro-apoptotic factors like AIF and cytochrome c, is dependent on the B-cell lymphoma 2 (BCL-2) family. Ischemic stroke causes upregulation of pro-apoptotic BCL-2 family members such as Bax, Bak, Bim, and Bid.[57] Interestingly, similar to AIF, cytochrome c can also translocate to the nucleus under conditions of cellular stress, where it changes chromatin structure by binding to histone chaperones.[58,59] However, the latter mechanism has not yet been studied in the context of ischemia/reperfusion injury. As discussed above, cytochrome c undergoes dephosphorylation during ischemia that clearly contributes to ETC hyperactivity, ROS, and cell death in the brain.[7,8,10]

In the context of ischemia reperfusion injury, we propose the following sequence of events that can be ameliorated with COX-inhibitory IRL: Ischemia leads to dephosphorylation of cytochrome c, its partner COX, and likely other ETC components, which primes the ETC for hyperactivity. Upon reperfusion, when oxygen and metabolites reenter the ischemic tissue, ETC resumes, and $\Delta\Psi_m$ hyperpolarization triggers an ROS burst at ETC complexes I and III,[45] which in turn initiates cell death cascades. COX-inhibitory IRL of 750-nm and 940-/950-nm light applied at the onset of reperfusion slows ETC flux, ameliorates $\Delta\Psi_m$ hyperpolarization, limits ROS generation, and is highly protective in animal models of brain ischemia/reperfusion injury, while COX-activating IRL showed no beneficial effect.[22,23] These findings indicate that different wavelengths of IRL can have very distinct effects on mitochondrial, cellular, and organismal function, which should be carefully considered.

Limiting ROS generation in stroke via IRL has the direct advantage of reducing a major source of cellular damage in a vulnerable neuron. Given the reliance on mitochondria and ROS signaling to engage the various downstream cell death signaling pathways, a secondary advantage offered by therapeutic IRL in stroke would be reducing activation of powerful feed-forward pathways that contribute to cell death. Altogether, this leads to robust neuroprotection.

5 | CONCLUSION

As we and others have shown, IRL therapy offers a promising and viable method to limit much of the damage from brain injuries. Both COX-inhibitory and -stimulatory IRL present unique therapeutic opportunities. However, for the treatment of pathological conditions, one must carefully consider the use of COX-inhibitory versus COX-activating IRL, and our data indicate that COX-inhibitory, but not COX-activating, IRL limits reperfusion injury. COX-inhibitory IRL applied during reperfusion has the advantage that it suppresses the production of ROS rather than scavenging them as

attempted with pharmacological approaches. In addition, it does not rely on blood flow and can thus be applied early during reperfusion, a time interval that cannot be covered with drugs delivered through the blood stream. Furthermore, therapeutic IRL is attractive because it is safe and can be applied noninvasively and locally directly to the desired tissue, limiting systemic side effects seen with pharmacological treatments. Our study is unique in that it uses fresh cadavers, suggesting that IRL penetration deeply into the human brain is feasible. Finally, skin pigmentation does not interfere with the two wavelengths studied here, making it a viable therapeutic approach independent of the patient's ethnicity.

ACKNOWLEDGMENTS

CONFLICT OF INTEREST

M.H. and T.H.S. are cofounders of Mitovation Inc. that develops infrared light therapy for ischemia/reperfusion injury applications. All other authors declare no potential conflict of interest.

ORCID

Paul T. Morse https://orcid.org/0000-0003-1530-1466
Maik Hüttemann https://orcid.org/0000-0001-6310-7081

REFERENCES

1. Johnson CO, Nguyen M, Roth GA, et al. Global, regional, and national burden of stroke, 1990–2016: A systematic analysis for the global burden of disease study 2016. Lancet Neurol. 2019; 18:439–458.

2. Benjamin EJ, Blaha MJ, Chiuve SE, et al. Heart disease and stroke Statistics-2017 update: A report from the American Heart Association. Circulation. 2017;135:e146–e603.

3. Benjamin EJ, Muntner P, Alonso A, et al. Heart disease and stroke Statistics-2019 update: A report from the American Heart Association. Circulation. 2019;139:e56–e528.

4. Hüttemann M, Lee I, Samavati L, Yu H, Doan JW. Regulation of mitochondrial oxidative phosphorylation through cell signaling. Biochim et Biophys Acta (BBA) Mol Cell Res. 2007;1773: 1701–1720.

5. Lo EH, Moskowitz MA, Jacobs TP. Exciting, radical, suicidal: How brain cells die after stroke. Stroke. 2005;36:189–192.

6. Kalpage HA, Wan J, Morse PT, et al. Cytochrome c phosphorylation: Control of mitochondrial electron transport chain flux and apoptosis. Int J Biochem Cell Biol. 2020;121:105704.

7. Kalpage HA, Vaishnav A, Liu J, et al. Serine-47 phosphorylation of cytochrome c in the mammalian brain regulates cytochrome c oxidase and caspase-3 activity. FASEB J. 2019;33: 13503–13514.

8. Kalpage HA, Wan J, Morse PT, Lee I, Hüttemann M. Brain-specific Serine-47 modification of cytochrome c regulates cytochrome c oxidase activity attenuating ROS production and cell death: Implications for ischemia/reperfusion injury and Akt signaling. Cells. 2020;9:1–18.

9. Chouchani ET, Pell VR, Gaude E, et al. Ischaemic accumulation of succinate controls reperfusion injury through mitochondrial ROS. Nature. 2014;515:431–435.

10. Guerra-Castellano A, Diaz-Moreno I, Velazquez-Campoy A, De la Rosa MA, Diaz-Quintana A. Structural and functional characterization of phosphomimetic mutants of cytochrome c at threonine 28 and serine 47. Biochim Biophys Acta. 1857;2016: 387–395.

11. Ogbi M, Johnson JA. Protein kinase Cepsilon interacts with cytochrome c oxidase subunit IV and enhances cytochrome c oxidase activity in neonatal cardiac myocyte preconditioning. Biochem J. 2006;393:191–199.

12. Fang JK, Prabu SK, Sepuri NB, et al. Site specific phosphorylation of cytochrome c oxidase subunits I, IVi1 and Vb in rabbit hearts subjected to ischemia/reperfusion. FEBS Lett. 2007;581: 1302–1310.

13. The RANTTAS Investigators. A randomized trial of tirilazad mesylate in patients with acute stroke (RANTTAS). Stroke. 1996;27:1453–1458.

14. van der Worp HB, de Haan P, Morrema E, Kalkman CJ. Methodological quality of animal studies on neuroprotection in focal cerebral ischaemia. J Neurol. 2005;252:1108–1114.

15. Liu RR, Murphy TH. Reversible cyclosporin A-sensitive mitochondrial depolarization occurs within minutes of stroke onset in mouse somatosensory cortex in vivo: A two-photon imaging study. J Biol Chem. 2009;284:36109–36117.

16. Hamblin MR. Photobiomodulation for traumatic brain injury and stroke. J Neurosci Res. 2018;96:731–743.

17. Jacques SL. Optical properties of biological tissues: A review. Phys Med Biol. 2013;58:R37–R61.

18. Karu T. Primary and secondary mechanisms of action of visible to near-IR radiation on cells. J Photochem Photobiol B. 1999; 49:1–17.

19. Wharton DC, Tzagoloff A. Studies on the Electron transfer system. Lvii. The near infrared absorption band of cytochrome oxidase. J Biol Chem. 1964;239:2036–2041.

20. Zivin JA, Sehra R, Shoshoo A, et al. NeuroThera(R) efficacy and safety Trial-3 (NEST-3): A double-blind, randomized, sham-controlled, parallel group, multicenter, pivotal study to assess the safety and efficacy of transcranial laser therapy with the NeuroThera(R) laser system for the treatment of acute

ischemic stroke within 24 h of stroke onset. Int J Stroke. 2014; 9:950–955.

21. Giacci MK, Wheeler L, Lovett S, et al. Differential effects of 670 and 830 nm red near infrared irradiation therapy: A comparative study of optic nerve injury, retinal degeneration, traumatic brain and spinal cord injury. PLoS One. 2014;9:e104565.

22. Sanderson TH, Wider JM, Lee I, et al. Inhibitory modulation of cytochrome c oxidase activity with specific near-infrared light wavelengths attenuates brain ischemia/reperfusion injury. Sci Rep. 2018;8:3481.

23. Strubakos CD, Malik M, Wider JM, et al. Non-invasive treatment with near-infrared light: A novel mechanisms-based strategy that evokes sustained reduction in brain injury after stroke. J Cereb Blood Flow Metab. 2019;40:833–844.

24. Rubira-Bullen IR, Rubira CM, Sarmento VA, Azevedo RA. Frontal sinus size on facial plain radiographs. J Morphol Sci. 2010;27:77–81.

25. Belaldavar C, Kotrashetti VS, Hallikerimath SR, Kale AD. Assessment of frontal sinus dimensions to determine sexual dimorphism among Indian adults. J Forensic Dent Sci. 2014;6: 25–30.

26. Eboh DEO, Ogbeide OU, Ivwighren T. Radiographic anthropometric study of frontal sinus for sex determination in Benin city, South-South Nigeria. J Forensic Dent Sci. 2017;9:31–35.

27. Jagdeo JR, Adams LE, Brody NI, Siegel DM. Transcranial red and near infrared light transmission in a cadaveric model. PLoS One. 2012;7:e47460.

28. Stolik S, Delgado JA, Pérez A, Anasagasti L. Measurement of the penetration depths of red and near infrared light in human "ex vivo" tissues. J Photochem Photobiol B: Biol. 2000;57: 90–93.

29. Johansson JD. Spectroscopic method for determination of the absorption coefficient in brain tissue. J Biomed Opt. 2010;15: 057005.

30. Samoilova KA, Bogacheva ON, Obolenskaya KD, Blinova MI, Kalmykova NV, Kuzminikh EV. Enhancement of the blood growth promoting activity after exposure of volunteers to visible and infrared polarized light. Part I: Stimulation of human keratinocyte proliferation in vitro. Photochem Photobiol Sci. 2004;3:96–101.

31. Henderson TA, Morries LD. Near-infrared photonic energy penetration: Can infrared phototherapy effectively reach the human brain? Neuropsychiatr Dis Treat. 2015;11:2191–2208.

32. Fukui Y, Ajichi Y, Okada E. Monte Carlo prediction of near-infrared light propagation in realistic adult and neonatal head models. Appl Opt. 2003;42:2881–2887.

33. Yaroslavsky AN, Schulze PC, Yaroslavsky IV, Schober R, Ulrich F, Schwarzmaier HJ. Optical properties of selected native and coagulated human brain tissues in vitro in the visible and near infrared spectral range. Phys Med Biol. 2002;47: 2059–2073.

34. Zhang L, Shi A, Lu H. Determination of optical coefficients of biological tissue from a single integrating-sphere. J Mod Opt. 2012;59:121–125.

35. Lampl Y, Zivin JA, Fisher M, et al. Infrared laser therapy for ischemic stroke: A new treatment strategy: Results of the NeuroThera effectiveness and safety Trial-1 (NEST-1). Stroke. 2007; 38:1843–1849.

36. Zivin JA, Albers GW, Bornstein N, et al. Effectiveness and safety of transcranial laser therapy for acute ischemic stroke. Stroke. 2009;40:1359–1364.

37. Ma S, Baillie LJ, Stringer MD. Reappraising the surface anatomy of the pterion and its relationship to the middle meningeal artery. Clin Anat. 2012;25:330–339.

38. Hwang K, Kim JH, Baik SH. Thickness map of parietal bone in Korean adults. J Craniofac Surg. 1997;8:208–212.

39. Pensler J, McCarthy JG. The calvarial donor site: An anatomic study in cadavers. Plast Reconstr Surg. 1985;75:648–651.

40. van Spronsen PH, Weijs WA, Valk J, Prahl-Andersen B, van Ginkel FC. Relationships between jaw muscle cross-sections and craniofacial morphology in normal adults, studied with magnetic resonance imaging. Eur J Orthod. 1991;13:351–361.

41. Ellis H, Mahadevan V. The surgical anatomy of the scalp. Surgery (Oxford). 2014;32:e1–e5.

42. Kolari PJ. Penetration of unfocused laser light into the skin. Arch Dermatol Res. 1985;277:342–344.

43. Kolari PJ, Airaksinen O. Poor penetration of infra-red and helium Neon low power laser light into the dermal tissue. Acupunct Electro-Ther Res. 1993;18:17–21.

44. Hüttemann M, Lee I, Pecinova A, Pecina P, Przyklenk K, Doan JW. Regulation of oxidative phosphorylation, the mitochondrial membrane potential, and their role in human disease. J Bioenerg Biomembr. 2008;40:445–456.

45. Sanderson TH, Reynolds CA, Kumar R, Przyklenk K, Hüttemann M. Molecular mechanisms of ischemia-reperfusion injury in brain: Pivotal role of the mitochondrial membrane potential in reactive oxygen species generation. Mol Neurobiol. 2013;47:9–23.

46. Hüttemann M, Helling S, Sanderson TH, et al. Regulation of mitochondrial respiration and apoptosis through cell signaling: Cytochrome c oxidase and cytochrome c in ischemia/reperfusion injury and inflammation. Biochim Biophys Acta. 1817;2012:598–609.

47. Goto S, Xue R, Sugo N, et al. Poly(ADP-ribose) polymerase impairs early and long-term experimental stroke recovery. Stroke. 2002;33:1101–1106.

48. Rodriguez-Vargas JM, Ruiz-Magana MJ, Ruiz-Ruiz C, et al. ROS-induced DNA damage and PARP-1 are required for optimal induction of starvation-induced autophagy. Cell Res. 2012; 22:1181–1198.

49. Pellegrini-Giampietro DE, Cherici G, Alesiani M, Carla V, Moroni F. Excitatory amino acid release and free radical formation may cooperate in the genesis of ischemia-induced neuronal damage. J Neurosci. 1990;10:1035–1041.

50. Chiarugi A. Poly(ADP-ribosyl)ation and stroke. Pharmacol Res. 2005;52:15–24.

51. Pleschke JM, Kleczkowska HE, Strohm M, Althaus FR. Poly (ADP-ribose) binds to specific domains in DNA damage checkpoint proteins. J Biol Chem. 2000;275:40974–40980.

52. Vaziri H, West MD, Allsopp RC, et al. ATM-dependent telomere loss in aging human diploid fibroblasts and DNA damage lead to the post-translational activation of p53 protein involving poly(ADP-ribose) polymerase. EMBO J. 1997;16:6018–6033.

53. Dawson VL, Dawson TM. Deadly conversations: Nuclear-mitochondrial cross-talk. J Bioenerg Biomembr. 2004;36: 287–294.

54. Komjáti K, Mabley J, Virág L, Southan G, Salzman A, Szabó C. Poly(ADP-ribose) polymerase inhibition protect neurons and the white matter and regulates the translocation of apoptosis-inducing factor in stroke. Int J Mol Med. 2004;13:373–382.

55. Cregan SP, Fortin A, MacLaurin JG, et al. Apoptosis-inducing factor is involved in the regulation of caspase-independent neuronal cell death. J Cell Biol. 2002;158:507–517.

56. Culmsee C, Zhu C, Landshamer S, et al. Apoptosis-inducing factor triggered by poly(ADP-ribose) polymerase and bid mediates neuronal cell death after oxygen-glucose deprivation and focal cerebral ischemia. J Neurosci. 2005;25:10262–10272.

57. Yang JL, Mukda S, Chen SD. Diverse roles of mitochondria in ischemic stroke. Redox Biol. 2018;16:263–275.

58. Gonzalez-Arzola K, Diaz-Moreno I, Cano-Gonzalez A, et al. Structural basis for inhibition of the histone chaperone activity of SET/TAF-Ibeta by cytochrome c. Proc Natl Acad Sci U S A. 2015;112:9908–9913.

59. Gonzalez-Arzola K, Diaz-Quintana A, Rivero-Rodriguez F, et al. Histone chaperone activity of *Arabidopsis thaliana* NRP1 is blocked by cytochrome c. Nucleic Acids Res. 2017;45: 2150–2165.